pcim
EUROPE

Highly Dynamic Voltage Control of a Dual Active Bridge over the Full Voltage Range by Operating Point Dependent Manipulated Variable Limitation

Georg Zieglmaier[1], Fabian Sommer[1], Tobias Merz[1], Marc Hiller[1]

[1] Institute of Electrical Engineering (ETI), Karlsruhe Institute of Technology (KIT), Germany

Corresponding author: Georg Zieglmaier, georg.zieglmaier@kit.edu
Speaker: Georg Zieglmaier, georg.zieglmaier@kit.edu

Abstract

This paper presents a highly dynamic voltage control for the Dual Active Bridge over the full operating range. Maximum dynamics is achieved by using the maximum available manipulated variable in combination with a feedforward control of the capacitor current at a setpoint change. Operation within the system limits is ensured by a variable limitation of the manipulated variable considering the current operating point. The simulation results are validated by measurements on a $35\,\mathrm{kW}$ Dual Active Bridge test bench.

1 Introduction

The Dual Active Bridge (DAB) has received significant attention in recent years due to its numerous advantages, including high power density, high efficiency, galvanic isolation, bidirectional power flow, and the capability of Zero Voltage Switching (ZVS) [1]. In addition, the DAB can operate at high frequencies, leading to smaller passive components, low audible switching noise and reduced size and weight of the overall system [2]. Since the DAB enables both buck and boost operation, it provides the capability to cover a wide voltage range, making it a versatile solution for a range of applications, such as interface for energy storage systems with a varying output voltage and switching topologies that use the DAB as a galvanically isolated and dynamically controllable voltage source [3][4].

The topology of the DAB, as shown in Fig. 1, consists of two full bridges with their AC terminals coupled by a Medium Frequency Transformer (MFT) with the transformation ratio n and the stray inductance L_σ. Via the full bridges the positive and negative DC link voltages $\pm V_1$ and $\pm V_2$ as well as $0\,\mathrm{V}$ can be set on each side of the MFT. For most modulation types and control strategies, the power semiconductors of the DAB are operated at the constant switching frequency f_s.

The most commonly used modulation type is Single

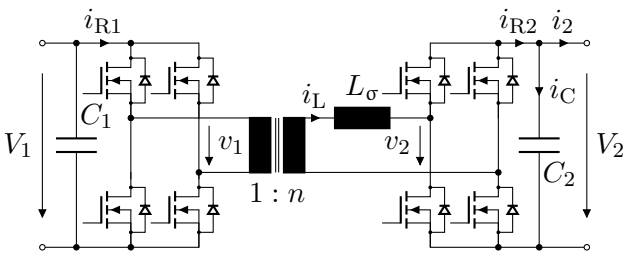

Fig. 1: Topology of the DAB

Phase Shift Modulation (SPSM), which applies a phase shift φ between the primary and secondary square wave voltages v_1 and v_2 to transmit a specified power P. More advanced modulation types that can reduce losses are the Dual Phase Shift Modulation (DPSM) and Triangular Current Mode Modulation (TCMM), which use the additional control angles δ_1 and δ_2 to influence the duty cycle of the square wave voltages v_1 and v_2 [5].

A precise and dynamic control strategy is essential to ensure optimal performance and reliable operation of the DAB. Various control strategies that rely on small-signal models have been proposed in the literature, as discussed in [6] and [7]. In these approaches, the DAB is linearized around a certain operating point and the control is based on the resulting small-signal model, thus limiting the control of the DAB around the linearized operating point.

The nonlinear control from [8] takes the approach of splitting the controller into a real-time linearization

stage and a linear control law, which also takes into account the large-signal behavior of the DAB. This allows operation over a wide voltage range, but the control dynamics are limited by the dynamics of the linearization, which is an order of magnitude lower than the switching frequency.

A control strategy that provides high dynamic response, fast transient behavior without overshoot and startup coverage is presented in [9]. This is a boundary control strategy using the natural switching surface of the DAB consisting of the secondary DC voltage V_2 and the transformer current i_L. However, the application of this strategy requires the measurement of the transformer current i_L. This is particularly challenging for systems with a low stray inductance L_σ, a high voltage range and thus a highly dynamic behavior, such as the DAB presented in [10].

The control strategy presented in this paper enables highly dynamic voltage control of the secondary DC voltage V_2 over the full operating range by using the maximum manipulated variable (MV) $\bar{i}_\mathrm{R2}$ in combination with feedforward control of the capacitor current i_C at a setpoint change. Stable operation within the system limits is ensured by an operating point dependent limitation of the MV. To operate the DAB over the full voltage range from $0\,\mathrm{V}$ to $V_{1,\max}$ and $V_{2,\max}$, the modulation types TCMM and SPSM are applied. For the application of this control strategy, only the measurement of the primary and secondary DC voltage V_1 and V_2 and knowledge of the system parameters L_σ and C_2 is required. To further increase the dynamics of the control, the load current i_2 can also be taken into account.

2 Control Model of the Dual Active Bridge and Control Structure

The calculation of the control angles for the modulation types TCMM and SPSM, based on [5], is done as a function of the mean rectified current $\bar{i}^*_\mathrm{R2}$ required on the secondary side. Assuming a loss-free and ideal behavior of the DAB, the MV $\bar{i}^*_\mathrm{R2}$ corresponds to the mean secondary rectified current $\bar{i}_\mathrm{R2}$ during one control period $T = \frac{1}{f_\mathrm{s}}$. These calculation steps, as well as the resulting gate driver signals for the power semiconductors, are shown in Fig. 2. In combination with the power semiconductors of the DAB and the MFT, which are represented by the blue block in Fig. 2, this results in the actuator for the controlled system. Given that the secondary DC voltage V_2 across the capacitor C_2 is the controlled variable, the system can be modeled by the equivalent circuit in Fig. 3. The actuator from Fig. 2 can be represented by a controlled current source with deadtime, which current is split into the capacitor current $\bar{i}_\mathrm{C}$ and the load current $\bar{i}_2$.

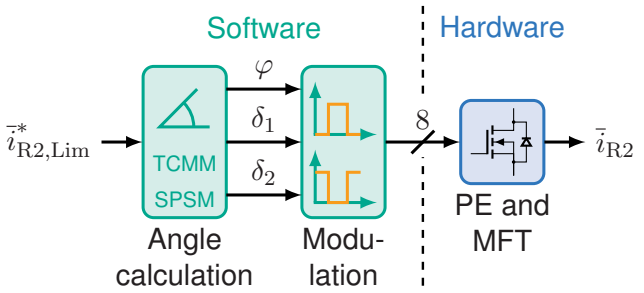

Fig. 2: Actuator of the DAB consisting of the calculation unit for the control angles, the modulation unit, the power electronics (PE) and the MFT

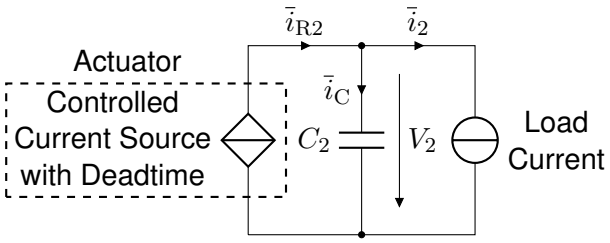

Fig. 3: Mean value model of the DAB as a controlled current source with deadtime

Based on the system model from Fig. 3, an integrating system behavior is obtained with the load current i_2 as an external disturbance. Taking into account the additional delays caused by the measurement units for the secondary DC voltage V_2 and the load current i_2, the controlled system can be represented as the blue framed part in the block diagram in Fig. 4. The area framed in red shows the structure of the voltage controller. Its individual aspects are explained in the following sections.

2.1 PI Controller Designed According to the Symmetrical Optimum

As a basis for the voltage controller, a PI controller is designed according to the symmetrical optimum [11]. This controller is mainly used to compensate for permanent control differences, parameter inaccuracies and non-linear behavior of the actuator resp. the PE with the MFT due to commutation effects of the DAB [12]. Since the dynamic control behavior is achieved by the controller extensions presented in the following, the PI controller can be

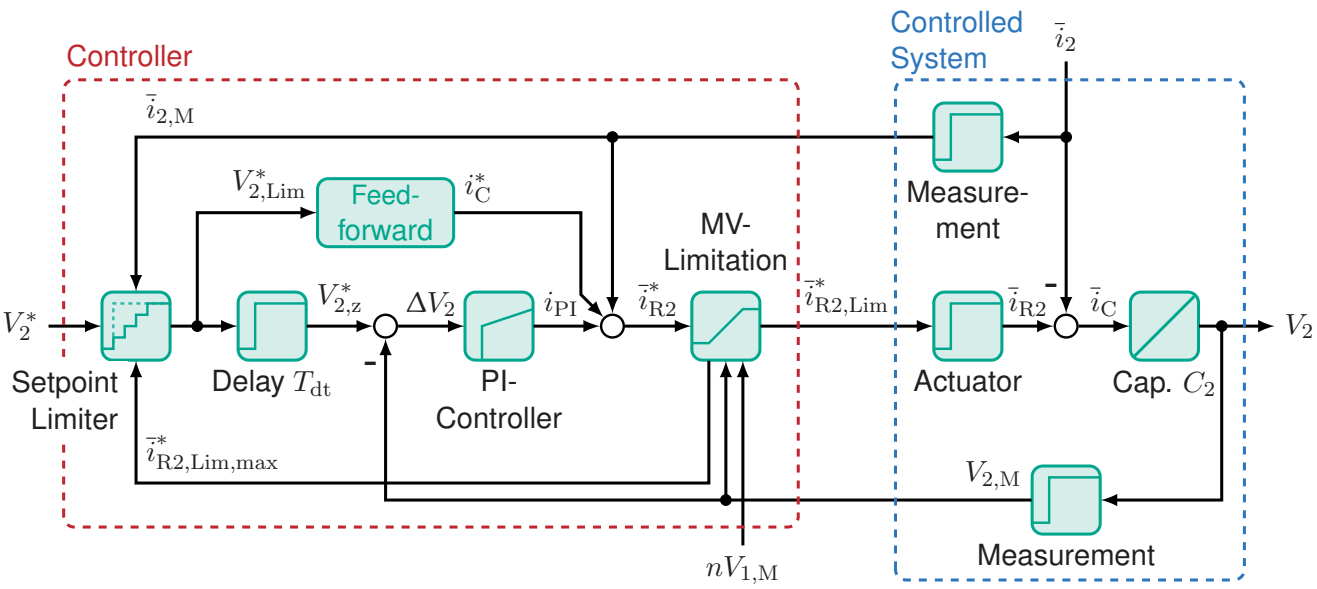

Fig. 4: Block diagram of the controlled system and the controller

designed for aperiodic transient response to ensure stability of the control even in the presence of larger parameter deviations.

2.2 Disturbance Feedforward Control of the Load Current

If a measurement of the load current $\bar{i}_{2,\mathrm{M}}$ is available or the load current i_2 is known from a higher-level application, it can be taken into account via a disturbance feedforward control. The load current $\bar{i}_2$ is added to the output of the PI controller i_PI in order to quickly adapt the $\bar{i}^*_\mathrm{R2}$ to a load change. Since the content of this paper mainly focuses on the reference response of the voltage control, load changes will not be discussed in the subsequent sections.

2.3 Manipulated Variable Limitation

To prevent damage to the system components caused by a large MV $\bar{i}^*_\mathrm{R2}$, a variable limitation of the MV is introduced. Five different system limits, given in Tab. 1, are considered, depending on the current primary and secondary DC voltage $V_{1,\mathrm{M}}$ and $V_{2,\mathrm{M}}$.

The first limiting criteria is the maximum transmittable power P_max of the system, which may be limited by both operation limits of system components and by systems connected to the DAB. The resulting maximum secondary current $\bar{i}_\mathrm{R2,max,P}$ is calculated according to Eq. (1).

$$|\bar{i}_\mathrm{R2,max,P}| = \frac{P_\mathrm{max}}{V_{2,\mathrm{M}}} \tag{1}$$

The second and third limiting criteria are the maximum mean primary and secondary rectified currents $\bar{i}_\mathrm{R1,max}$ and $\bar{i}_\mathrm{R2,max}$, which must be limited, for example, due to sensors or systems connected to the DAB.

Since all variables of the control are related to the secondary side of the DAB, the maximum rectified primary current $\bar{i}_\mathrm{R2,max,i1}$ must be converted to the secondary side according to Eq. (2). Conversion of the maximum rectified secondary current $\bar{i}_\mathrm{R2,max}$ is therefore not necessary.

$$|\bar{i}_\mathrm{R2,max,i1}| = \frac{nV_{1,\mathrm{M}}}{V_{2,\mathrm{M}}} \cdot \bar{i}_\mathrm{R1,max} \tag{2}$$

Due to the characteristics of the used modulation types TCMM and SPSM, the transmittable power P and thus the secondary rectified current $\bar{i}_\mathrm{R2}$ is limited [5]. The calculation for TCMM is done according to Eq. (3) and for SPSM according to Eq. (4).

$$|\bar{i}_\mathrm{R2,max,TCMM}| = \begin{cases} \dfrac{(V_{2,\mathrm{M}} - nV_{1,\mathrm{M}}) \cdot (nV_{1,\mathrm{M}})^2}{4L_\sigma f_\mathrm{s} V_{2,\mathrm{M}}^2} & , nV_{1,\mathrm{M}} < V_{2,\mathrm{M}} \\ \dfrac{(nV_{1,\mathrm{M}} - V_{2,\mathrm{M}}) \cdot V_{2,\mathrm{M}}}{4L_\sigma f_\mathrm{s} nV_{1,\mathrm{M}}} & , nV_{1,\mathrm{M}} > V_{2,\mathrm{M}} \end{cases} \tag{3}$$

$$|\bar{i}_\mathrm{R2,max,SPSM}| = \frac{nV_{1,\mathrm{M}}}{8L_\sigma f_\mathrm{s}} \tag{4}$$

As the last system limit considered here, the transformer current i_L must not exceed the maximum

value $\hat{i}_{\mathrm{L,max}}$ to prevent damage to the system components such as the power semiconductors due to maximum switching currents or the current sensors due to maximum measurable currents. The calculation of the resulting maximum MV $\bar{i}_{\mathrm{R2,max,L}}$ as a function of the maximum transformer current $\hat{i}_{\mathrm{L,max}}$ set by the user is based on the steady-state current waveforms for TCMM and SPSM [5].
The results for TCMM and SPSM are given in Eq. (5) and Eq. (6), respectively.

$$|\bar{i}_{\mathrm{R2,max,L,TCMM}}| = \begin{cases} \dfrac{L_\sigma f_\mathrm{s} \hat{i}_{\mathrm{L,max}}{}^2}{V_{2,\mathrm{M}} - nV_{1,\mathrm{M}}} & , nV_{1,\mathrm{M}} < V_{2,\mathrm{M}} \\ \dfrac{L_\sigma f_\mathrm{s} \hat{i}_{\mathrm{L,max}}{}^2}{nV_{1,\mathrm{M}} - V_2} \cdot \dfrac{nV_{1,\mathrm{M}}}{V_{2,\mathrm{M}}} & , nV_{1,\mathrm{M}} > V_{2,\mathrm{M}} \end{cases} \tag{5}$$

$$|\bar{i}_{\mathrm{R2,max,L,SPSM}}| = \frac{nV_{1,\mathrm{M}}}{8L_\sigma f_\mathrm{s}} \cdot \begin{cases} 1 - \dfrac{\left(V_{2,\mathrm{M}} - 4L_\sigma f_\mathrm{s} \cdot \min\left[\hat{i}_{\mathrm{L,max}}, \frac{V_{2,\mathrm{M}}}{4L_\sigma f_\mathrm{s}}\right]\right)^2}{(nV_{1,\mathrm{M}})^2} & , nV_{1,\mathrm{M}} \leq V_{2,\mathrm{M}} \\ 1 - \dfrac{\left(nV_{1,\mathrm{M}} - 4L_\sigma f_\mathrm{s} \cdot \min\left[\hat{i}_{\mathrm{L,max}}, \frac{nV_{1,\mathrm{M}}}{4L_\sigma f_\mathrm{s}}\right]\right)^2}{V_{2,\mathrm{M}}{}^2} & , nV_{1,\mathrm{M}} > V_{2,\mathrm{M}} \end{cases} \tag{6}$$

The five system limits considered in the variable limitation of the MV are summarized in Tab. 1 along with their corresponding equations.

	Limiting Reason	MV Limit	Equation
(a)	$P_{\max}$	$\bar{i}_{\mathrm{R2,max,P}}$	Eq. (1)
(b)	$\bar{i}_{\mathrm{R1,max}}$	$\bar{i}_{\mathrm{R2,max,i1}}$	Eq. (2)
(c)	$\bar{i}_{\mathrm{R2,max}}$	$\bar{i}_{\mathrm{R2,max}}$	By definition
(d)	Modulation	$\bar{i}_{\mathrm{R2,max,TCMM}}$ $\bar{i}_{\mathrm{R2,max,SPSM}}$	TCMM: Eq. (3) SPSM: Eq. (4)
(e)	$\hat{i}_{\mathrm{L,max}}$	$\bar{i}_{\mathrm{R2,max,L,TCMM}}$ $\bar{i}_{\mathrm{R2,max,L,SPSM}}$	TCMM: Eq. (5) SPSM: Eq. (6)

Tab. 1: Considered limits for the MV limitation with the respective equations

An anti windup is implemented in the controller structure to prevent windup behavior of the PI controller when the limitation of the MV is active. For reasons of clarity, the anti windup is not shown in Fig. 4.

2.3.1 Active Limitation of the Manipulated Variable Depending on the Current Operating Point

In addition to the limiting reasons from Tab. 1, the individual MV limits are only dependent on the current primary and secondary DC voltage $V_{1,\mathrm{M}}$ and $V_{2,\mathrm{M}}$. When limited by the modulation type (d) or the transformer current $\hat{i}_{\mathrm{L,max}}$ (e), the limit which allows the higher secondary current $\bar{i}_{\mathrm{R2}}$ is selected first. This ensures that the modulation type is selected which can set the required MV $\bar{i}^*_{\mathrm{R2}}$ within the specified limits. To determine the active MV limitation, the individual limiting variables are then compared with each other at the current operating

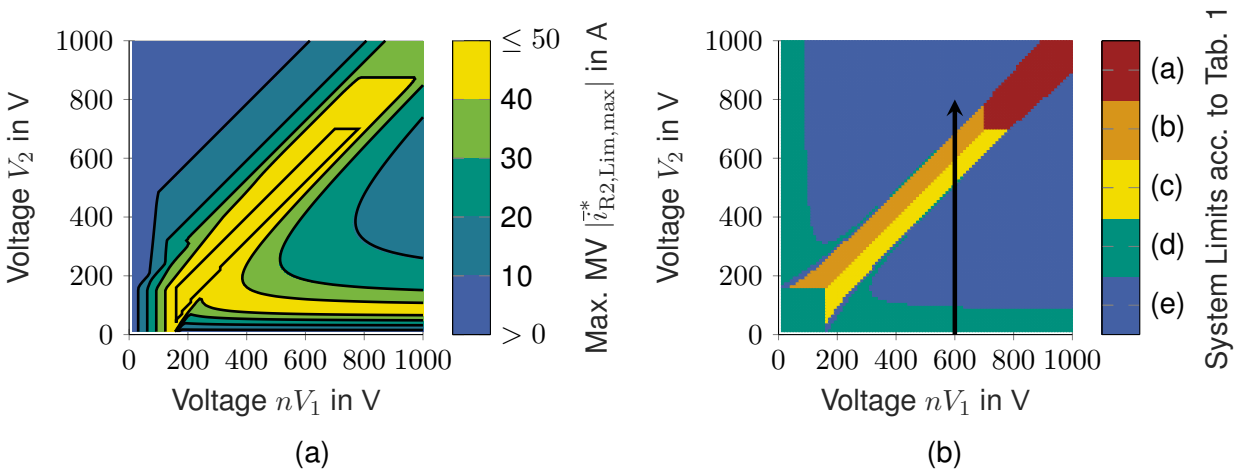

Fig. 5: The maximum MV $\bar{i}^*_{\mathrm{R2,Lim,max}}$ in (a) and the system limit regions in (b) are plotted against the converted primary DC voltage nV_1 and secondary DC voltage V_2

point. The MV limitation with the smallest permitted secondary current is selected. This selection process is summarized in Eq. (7).

$$
\begin{aligned}
&|\bar{i}^*_{\mathrm{R2,Lim,max}}| = \\
&\min\Big[\bar{i}_{\mathrm{R2,max,P}}, \bar{i}_{\mathrm{R2,max,i1}}, \bar{i}_{\mathrm{R2,max}}, \\
&\quad \max\left[\bar{i}_{\mathrm{R2,max,TCMM}}, \bar{i}_{\mathrm{R2,max,SPSM}}\right], \\
&\quad \max\left[\bar{i}_{\mathrm{R2,max,L,TCMM}}, \bar{i}_{\mathrm{R2,max,L,SPSM}}\right]\Big]
\end{aligned}
\tag{7}
$$

The resulting maximum value $\bar{i}^*_{\mathrm{R2,Lim}}$ of the MV is shown over the entire DC voltage range of V_1 and V_2 in Fig. 5a for the DAB with the parameters given in Tab. 2. The regions in which the respective MV limitation from Tab. 1 is active is shown in Fig. 5b. It can be seen from Fig. 5a that a MV $|\bar{i}^*_{\mathrm{R2,Lim}}| > 0\,\mathrm{A}$ can be set over the entire voltage range of the primary and secondary DC voltage V_1 and V_2 without exceeding any of the system limits. This enables control of the secondary DC voltage V_2 at any constellation between the primary and secondary DC voltage, eliminating the need for an additional precharging process of the secondary side capacitor C_2.
The arrow in Fig. 5b shows the path along the different MV limitations for a setpoint change from $V_2^* = 0\,\mathrm{V}$ to $800\,\mathrm{V}$ at $nV_1 = 600\,\mathrm{V}$, which simulation and measurement results are discussed in section 4.

2.3.2 Maximum Transmittable Power

By multiplying the maximum value $\bar{i}^*_{\mathrm{R2,Lim,max}}$ of the MV by the secondary DC voltage V_2 at the respective operating point, the maximum transmittable power $P_{\max}$ at each operating point can be calculated. For the DAB with its parameters given in Tab. 2 and used for the measurements in section 4, the maximum transmittable power $P_{\max}$ as a function of the converted primary DC voltage nV_1 and secondary DC voltage V_2 is shown in Fig. 7.

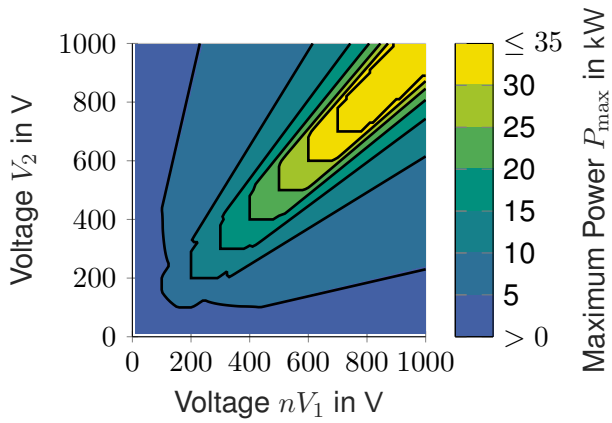

Fig. 7: Maximum transmittable power $P_{\max}$ plotted against the converted primary DC voltage nV_1 and secondary DC voltage V_2

2.4 Modification of the Setpoint Change considering the Manipulated Variable Limitation

By the limitation of the MV $\bar{i}^*_{\mathrm{R2}}$ to a maximum MV $\bar{i}^*_{\mathrm{R2,Lim,max}}$, the maximum voltage change of the secondary DC voltage V_2 within one control period T is limited as well. This information can be used to limit the setpoint change $\Delta V^*_{2,\mathrm{Lim}} = V^*_{2,\mathrm{Lim}} - V^*_{2,\mathrm{Lim,z}}$ per control period T in such a way that the MV $\bar{i}^*_{\mathrm{R2}}$ is completely utilized, but not exceeded. In the following sections, this controller part is referred to as the setpoint limiter. The corresponding block diagram is shown in Fig. 6. The variable $V^*_{2,\mathrm{Lim}}$ describes the limited setpoint of the current control period and variable $V^*_{2,\mathrm{Lim,z}}$ describes the setpoint

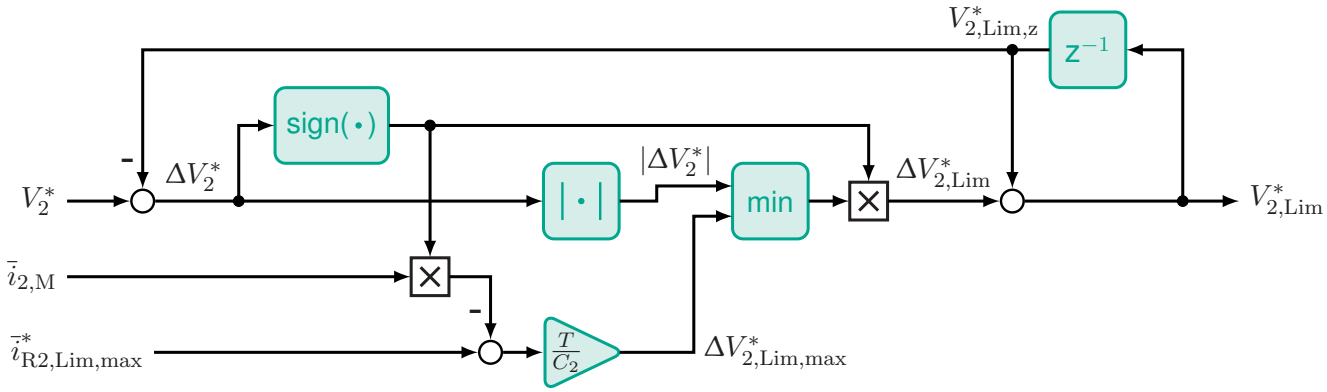

Fig. 6: Block diagram of the setpoint limiter

of the previous control period.
The maximum possible setpoint change $\Delta V^*_{2,\mathrm{Lim,max}}$ is calculated according to Eq. (8), taking into account the measured load current $\bar{i}_{2,\mathrm{M}}$, the maximum MV $\bar{i}^*_{\mathrm{R2,Lim,max}}$ and the sign of the remaining setpoint change $\Delta V^*_2 = V^*_2 - V^*_{2,\mathrm{Lim,z}}$.

$$\Delta V^*_{2,\mathrm{Lim,max}} = \frac{T}{C_2} \cdot \left(\bar{i}^*_{\mathrm{R2,Lim,max}} - \mathrm{sign}(\Delta V^*_2) \cdot \bar{i}_{2,\mathrm{M}}\right) \tag{8}$$

If the remaining setpoint difference ΔV^*_2 is greater than the maximum possible setpoint change $\Delta V^*_{2,\mathrm{Lim,max}}$, then $\Delta V^*_{2,\mathrm{Lim,max}}$ is added or subtracted from the setpoint of the previous control period $V^*_{2,\mathrm{Lim,z}}$. If the remaining setpoint difference ΔV^*_2 is smaller than the maximum possible setpoint change $\Delta V^*_{2,\mathrm{Lim,max}}$, then the setpoint V^*_2 can be reached within one control period T and the remaining setpoint difference ΔV^*_2 is added or subtracted from the setpoint of the last control period $V^*_{2,\mathrm{Lim,z}}$. Whether an addition or subtraction of the setpoint change from the setpoint of the last control period $V^*_{2,\mathrm{Lim,z}}$ takes place depends on the sign of the remaining setpoint difference ΔV^*_2.
The calculation of the limited setpoint $V^*_{2,\mathrm{Lim}}$ is summarized in Eq. (9).

$$\begin{aligned} V^*_{2,\mathrm{Lim}} = {} & V^*_{2,\mathrm{Lim,z}} + \\ & \mathrm{sign}(\Delta V^*_2) \cdot \min\left[|\Delta V^*_2|, \Delta V^*_{2,\mathrm{Lim,max}}\right] \end{aligned} \tag{9}$$

2.5 Feedforward Control of the Capacitor Charge Current

For a setpoint change of the secondary DC voltage $\Delta V^*_{2,\mathrm{Lim}} = V^*_{2,\mathrm{Lim}} - V^*_{2,\mathrm{Lim,z}}$ given by the setpoint limiter, the capacitor current i^*_{C} from Eq. (10) is required in order to reach the desired voltage $V^*_{2,\mathrm{Lim}}$ within one control period T.

$$i^*_{\mathrm{C}} = \frac{C_2}{T} \cdot \Delta V^*_{2,\mathrm{Lim}} \tag{10}$$

The current i^*_{C} is added to the current i_{PI} at the output of the PI controller via the feedforward control, which is shown in Fig. 8. The feedforward controller behaves like an ideal D element and would only be active in the control period of a setpoint change. Due to a successive adjustment of the setpoint $V^*_{2,\mathrm{Lim}}$ by the setpoint limiter, the feedforward control is active until the required setpoint V^*_2 is reached.

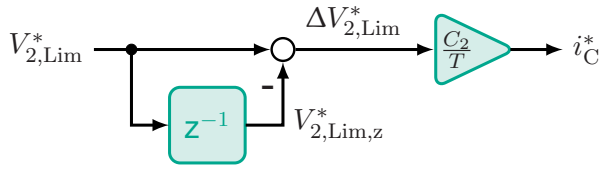

Fig. 8: Block diagram of the feedforward control

As seen in Fig. 4, the feedback of the measured secondary DC voltage $V_{2,\mathrm{M}}$ occurs with the total deadtime T_{dt} due to the deadtime of the PE and the measurement. Therefore the setpoint $V^*_{2,\mathrm{Lim}}$ must also be delayed by the deadtime T_{dt}. With ideal feedforward control of the capacitor current i_{C}, the PI controller observes no difference between the delayed setpoint voltage $V^*_{2,\mathrm{z}}$ and the measured voltage $V_{2,\mathrm{M}}$. Consequently, intervention by the PI controller only takes place in case of parameter deviations and to achieve stationary accuracy.
In addition, the combination of the setpoint limiter and the feedforward control allows full utilization of the available MV $\bar{i}^*_{\mathrm{R2}}$ to its limit in each control period, which means a maximum dynamic voltage change can be achieved without violating the system limits.

3 Experimental Setup

This chapter briefly describes the DAB and MFT hardware depicted in Fig. 9 and the setup of the corresponding test bench used to validate the proposed voltage control. The associated parameters and the system limits relevant for the control are listed in Tab. 2.

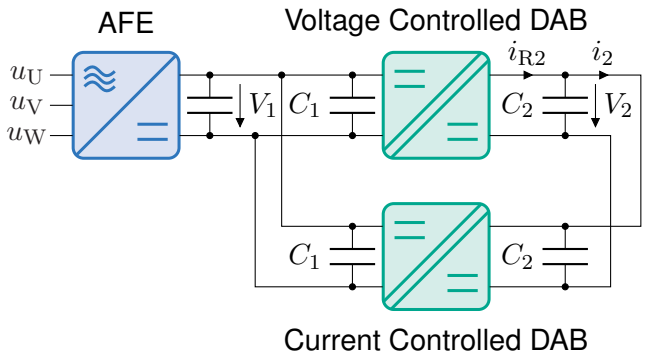

Fig. 10: Setup of the DAB test bench

An overview diagram of the test bench consisting of an Active Front End (AFE) and two DABs is shown in Fig. 10. The AFE provides power to the test bench and is responsible for controlling the voltage V_1 of the common DC link between the AFE and

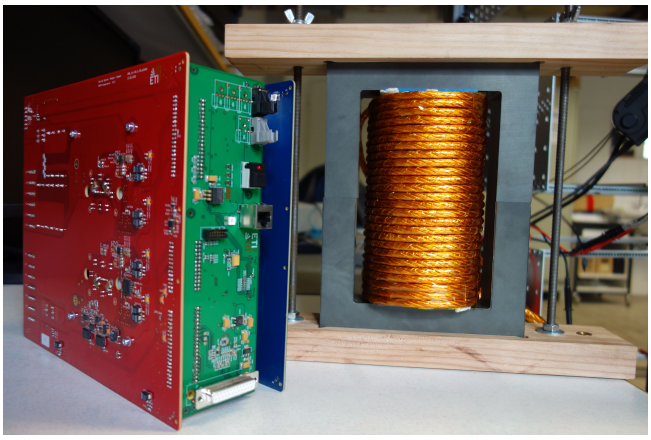

Fig. 9: DAB power electronics with the MFT

Parameter	Value
L_σ	7.7 µH
n	1
f_s	50 kHz
P_max	35 kW
$\hat{i}_\mathrm{L,max}$	100 A
$\bar{i}_\mathrm{R1,max}$	50 A
$\bar{i}_\mathrm{R2,max}$	50 A
$V_\mathrm{1,max}$	850 V
$V_\mathrm{2,max}$	850 V

Tab. 2: Parameters of the DAB

both DABs. The DAB at the bottom of Fig. 10 is current controlled and is used to set the load current i_2 on the secondary side of the DABs. The upper DAB is used to test the proposed control of the voltage V_2.
A more detailed description of the hardware is given in [13], where the DAB and AFE are used for a standardized and modular power electronics platform for academic research.
In order to ensure the realtime capability of the control, the implementation is done on the Field Programmable Gate Array (FPGA) of the DAB. The signal processing developed at the institute, which is presented in [14], is used as central control unit for the test bench and to provide the setpoints for the voltage and current control.

4 Simulation and Measurement Results

In this chapter, the results from a PLECS® simulation model in MATLAB/Simulink® are compared with the measured data from the test bench to validate the presented control strategy and its realtime capable implementation on the DAB's FPGA. In addition to the output voltage V_2, the maximum amplitude of the transformer current $|\hat{i}_\mathrm{L}|$ is measured in each control period T to monitor the operation of the DAB within the system limits. Before a voltage setpoint change is applied to the DAB at time $t = 0\,\mathrm{s}$, the DAB is in a steady-state operating condition. The load current i_2 is constant during the setpoint change. At all operating points, a constant primary voltage of $V_1 = 600\,\mathrm{V}$ is set by the AFE.
The startup process of the DAB with a setpoint change from $V_2^* = 0\,\mathrm{V}$ to $800\,\mathrm{V}$ at no load is shown in Fig. 11. This voltage change corresponds to the black arrow in Fig. 5b.
The background in Fig. 11 is colored according to the active MV limitation from Tab. 1. It can be seen that at the beginning the maximum current in TCMM is the limiting variable and both the secondary DC voltage V_2 and the amplitude of the transformer current $|\hat{i}_\mathrm{L}|$ increase. As soon as the amplitude of the transformer current $|\hat{i}_\mathrm{L}|$ reaches the limit of $\hat{i}_\mathrm{L,max} = 100\,\mathrm{A}$, this system limit becomes active. The MV $\bar{i}^*_\mathrm{R2,Lim}$ is adjusted to this limit and thus the amplitude of the transformer current $|\hat{i}_\mathrm{L}|$ does not exceed $\hat{i}_\mathrm{L,max} = 100\,\mathrm{A}$ in the following time interval. In the area from $V_2 = 500\,\mathrm{V}$ to $700\,\mathrm{V}$ the rectifier currents on the primary and secondary side $\bar{i}_\mathrm{R1,max}$ and $\bar{i}_\mathrm{R2,max}$ are the limiting variables. Above a voltage of $V_2 = 700\,\mathrm{V}$, the MV $\bar{i}^*_\mathrm{R2,Lim}$ is again limited by the maximum amplitude of the transformer current $\hat{i}_\mathrm{L,max}$. By using the setpoint limiter in combination with the feedforward control, no overshoot after reaching the setpoint V_2^* is noticeable. Only minor differences between the simulation and measurement results can be identified, which can be explained by parameter deviations and non-linear effects of the DAB [12].
In the following plots, measurements of a PI controller designed according to the symmetric optimum without a MV limitation are used as reference to the proposed control structure.
Figure 12 shows the simulation and measurement results on the test bench for a setpoint change from $V_2^* = 400\,\mathrm{V}$ to $500\,\mathrm{V}$ at a load current of $i_2 = 15\,\mathrm{A}$. It can be seen that the reference controller has a faster rise time, but a slower settling time with overshoot behavior compared to the new control structure, proposed in this paper. The response

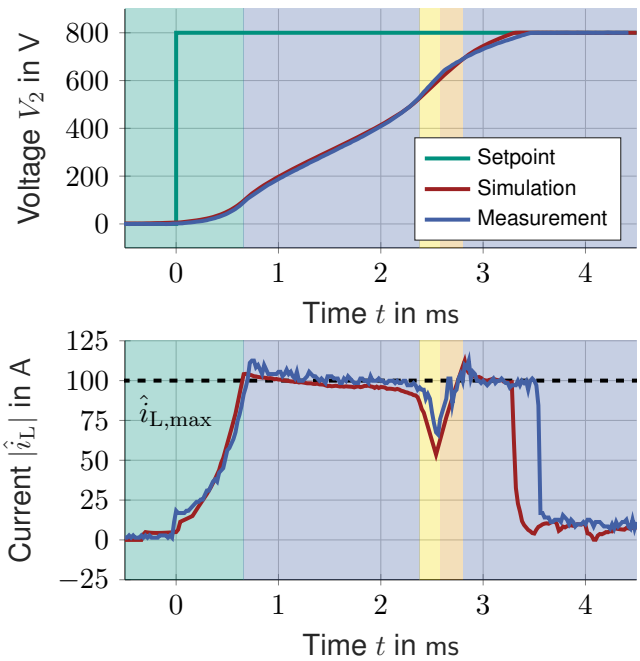

Fig. 11: Voltage setpoint change V_2^* with the corresponding peak value of the transformer current $|\hat{i}_L|$ from $V_2^* = 0\,\mathrm{V}$ to $800\,\mathrm{V}$ at load current $i_2 = 0\,\mathrm{A}$

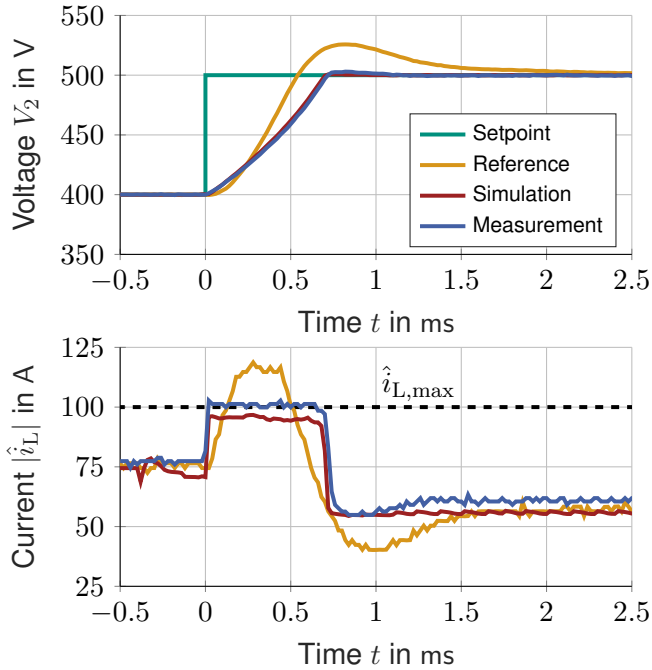

Fig. 12: Voltage setpoint change V_2^* with the corresponding peak value of the transformer current $|\hat{i}_L|$ from $V_2^* = 400\,\mathrm{V}$ to $500\,\mathrm{V}$ at load current $i_2 = 15\,\mathrm{A}$

time of the new control structure is faster compared to the reference controller due to the feedforward control of the capacitor current i_C, which becomes active in the event of a setpoint change. In addition, the reference controller exceeds the limit of the maximum transformer current $\hat{i}_{L,max}$, whereas the new control structure fully utilizes the MV $\bar{i}_{R2}^*$ over the course of the voltage change without exceeding any of the system limits.

In Fig. 13 and Fig. 14, the reference controller and the new control structure are compared for a setpoint change from $V_2^* = 400\,\mathrm{V}$ to $700\,\mathrm{V}$ with a load current of $i_2 = 15\,\mathrm{A}$ and $-15\,\mathrm{A}$. This comparison shows the influence of the load current i_2 on the control dynamics. With a positive load current, the secondary current $\bar{i}_{R2}$ is divided into the load current i_2 and the capacitor current $\bar{i}_C$, which limits the dynamics of the voltage change. With a negative load current, both the secondary current $\bar{i}_{R2}$ and the load current i_2 are used to charge the capacitor C_2, increasing the dynamics of the voltage change. This is not taken into account in the reference controller, which means that the dynamics remain approximately the same, but either a violation of the system limits occurs in the case of $i_2 = 15\,\mathrm{A}$ or the available dynamics are not fully utilized and a higher overshoot occurs in the case of $i_2 = -15\,\mathrm{A}$.

5 Conclusion

This paper presents a novel highly dynamic voltage control strategy with a variable limitation of th manipulated variable. For the derivation of the control structure, a system model of the DAB is presented. By taking into account different system limits, operation of the Dual Active Bridge is enabled over the full voltage range from $0\,\mathrm{V}$ to the maximum voltage utilizing the maximum permitted manipulated variable. The feedforward control of the capacitor current in combination with the variable limitation of the manipulated variable and the setpoint limiter allow for maximum dynamics of the voltage control at any operating point. Simulation and measurement results are presented to validate the behavior of the control structure and the realtime capability of the implementation on an FPGA. Slight deviations are due to neglected nonlinear effects of the DAB as well as parameter deviations. In addition, a comparison of the new control structure with a reference controller shows that operation within the system limits is guaranteed and that dynamic system behavior can be further improved by taking into account the load current.

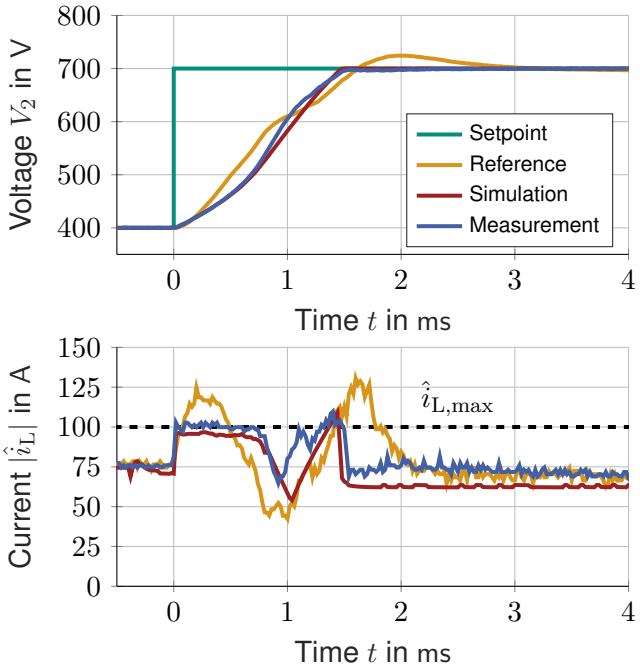

Fig. 13: Voltage setpoint change V_2^* with the corresponding peak value of the transformer current $|\hat{i}_L|$ from $V_2^* = 400\,\mathrm{V}$ to $700\,\mathrm{V}$ at load current $i_2 = 15\,\mathrm{A}$

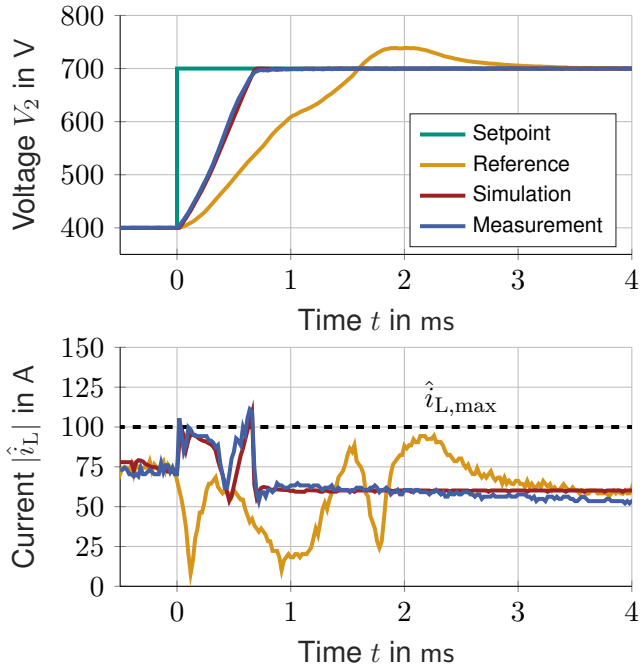

Fig. 14: Voltage setpoint change V_2^* with the corresponding peak value of the transformer current $|\hat{i}_L|$ from $V_2^* = 400\,\mathrm{V}$ to $700\,\mathrm{V}$ at load current $i_2 = -15\,\mathrm{A}$

References

[1] R. De Doncker, D. Divan, and M. Kheraluwala, "A three-phase soft-switched high-power-density DC/DC converter for high-power applications," *IEEE Transactions on Industry Applications*, vol. 27, no. 1, pp. 63–73, 1991. DOI: 10.1109/28.67533.

[2] B. Zhao, Q. Song, W. Liu, and Y. Sun, "Overview of Dual-Active-Bridge Isolated Bidirectional DCDC Converter for High-Frequency-Link Power-Conversion System," *IEEE Transactions on Power Electronics*, vol. 29, no. 8, pp. 4091–4106, 2014. DOI: 10.1109/TPEL.2013.2289913.

[3] N. Tan, S. Inoue, A. Kobayashi, and H. Akagi, "Voltage Balancing of a 320-V, 12-F Electric Double-Layer Capacitor Bank Combined With a 10-kW Bidirectional Isolated DC–DC Converter," *IEEE Transactions on Power Electronics*, vol. 23, no. 6, pp. 2755–2765, 2008. DOI: 10.1109/TPEL.2008.2005388.

[4] N. Menger, T. Merz, J. Gehringer, F. Sommer, and M. Hiller, "Loss Estimation of a Dual Active Bridge as part of a Solid State Transformer using Frequency Domain Modelling," in *2022 IEEE Energy Conversion Congress and Exposition (ECCE)*, 2022, pp. 1–8. DOI: 10.1109/ECCE50734.2022.9947488.

[5] N. Schibli, "Symmetrical multilevel converters with two quadrant DC-DC feeding," Dissertation, École polytechnique fédérale de Lausanne, 2000.

[6] H. Qin and J. W. Kimball, "Generalized Average Modeling of Dual Active Bridge DCDC Converter," *IEEE Transactions on Power Electronics*, vol. 27, no. 4, pp. 2078–2084, 2012. DOI: 10.1109/TPEL.2011.2165734.

[7] F. Krismer and J. W. Kolar, "Accurate Small-Signal Model for the Digital Control of an Automotive Bidirectional Dual Active Bridge," *IEEE Transactions on Power Electronics*, vol. 24, no. 12, pp. 2756–2768, 2009. DOI: 10.1109/TPEL.2009.2027904.

[8] D. D. M. Cardozo, J. C. Balda, D. Trowler, and H. A. Mantooth, "Novel nonlinear control of Dual Active Bridge using simplified converter model," in *2010 Twenty-Fifth Annual IEEE Applied Power Electronics Conference and Exposition (APEC)*, 2010, pp. 321–327. DOI: 10.1109/APEC.2010.5433651.

[9] G. G. Oggier, M. Ordonez, J. M. Galvez, and F. Luchino, "Fast Transient Boundary Control and Steady-State Operation of the Dual Active Bridge Converter Using the Natural Switching Surface," *IEEE Transactions on Power Electronics*, vol. 29, no. 2, pp. 946–957, 2014. DOI: 10.1109/TPEL.2013.2256150.

[10] F. Sommer, N. Menger, T. Merz, N. Soltau, S. Idaka, and M. Hiller, “Design and Characterization of a 500 kW 20 kHz Dual Active Bridge using 1.2 kV SiC MOSFETs,” in *2022 International Power Electronics Conference (IPEC-Himeji 2022- ECCE Asia)*, 2022, pp. 1390–1397. DOI: 10.23919/IPEC-Himeji2022-ECCE53331.2022.9807023.

[11] C. L. Kessler, “Das Symmetrische Optimum, Teil I,” *at - Automatisierungstechnik*, vol. 6, no. 1-12, pp. 395–400, 1958. DOI: doi:10.1524/auto.1958.6.112.395.

[12] F. Sommer, N. Menger, T. Merz, N. Soltau, S. Idaka, and M. Hiller, “Time Domain Modeling of Zero Voltage Switching behavior considering Parasitic Capacitances for a Dual Active Bridge,” in *11th International Conference on Power Electronics ECCE Asia (ICPE 2023-ECCE Asia)*, preprint, 2023.

[13] S. R. Frank, D. Schulz, L. Stefanski, R. Schwendemann, and M. Hiller, “A standardized and modular power electronics platform for academic research on advanced grid-connected converter control and microgrids,” in *2022 24th European Conference on Power Electronics and Applications (EPE’22 ECCE Europe)*, 2022, pp. 1–9.

[14] B. Schmitz-Rode, L. Stefanski, R. Schwendemann, S. Decker, S. Mersche, *et al.*, “A modular signal processing platform for grid and motor control, HIL and PHIL applications,” in *2022 International Power Electronics Conference (IPEC-Himeji 2022- ECCE Asia)*, 2022, pp. 1817–1824. DOI: 10.23919/IPEC-Himeji2022-ECCE53331.2022.9807061.